

An asymmetric dust ring around a very low mass star ZZ Tau IRS

JUN HASHIMOTO ^{1,2,3} RUOBING DONG ⁴ AND TAKAYUKI MUTO⁵

¹*Astrobiology Center, National Institutes of Natural Sciences, 2-21-1 Osawa, Mitaka, Tokyo 181-8588, Japan*

²*Subaru Telescope, National Astronomical Observatory of Japan, Mitaka, Tokyo 181-8588, Japan*

³*Department of Astronomy, School of Science, Graduate University for Advanced Studies (SOKENDAI), Mitaka, Tokyo 181-8588, Japan*

⁴*Department of Physics & Astronomy, University of Victoria, Victoria, BC, V8P 1A1, Canada*

⁵*Division of Liberal Arts, Kogakuin University, 1-24-2, Nishi-Shinjuku, Shinjuku-ku, Tokyo 163-8677, Japan*

ABSTRACT

We present Atacama Large Millimeter/submillimeter Array (ALMA) gas and dust observations at band 7 (339 GHz: 0.89 mm) of the protoplanetary disk around a very low mass star ZZ Tau IRS with a spatial resolution of $0''.25$. The $^{12}\text{CO } J = 3 \rightarrow 2$ position–velocity diagram suggests a dynamical mass of ZZ Tau IRS of $\sim 0.1\text{--}0.3 M_{\odot}$. The disk has a total flux density of 273.9 mJy, corresponding to an estimated mass of $24\text{--}50 M_{\oplus}$ in dust. The dust emission map shows a ring at $r = 58$ au and an azimuthal asymmetry at $r = 45$ au with a position angle of 135° . The properties of the asymmetry, including radial width, aspect ratio, contrast, and contribution to the total flux, were found to be similar to the asymmetries around intermediate mass stars ($\sim 2 M_{\odot}$) such as MWC 758 and IRS 48. This implies that the asymmetry in the ZZ Tau IRS disk shares a similar origin with others, despite the star being ~ 10 times less massive. Our observations also suggest that the inner and outer parts of the disk may be misaligned. Overall, the ZZ Tau IRS disk shows evidence of giant planet formation at ~ 10 au scale at a few Myr. If confirmed, it will challenge existing core accretion models, in which such planets have been predicted to be extremely hard to form around very low mass stars.

Keywords: protoplanetary disks — planet–disk interactions — planets and satellites: formation — stars: individual (ZZ Tau IRS)

1. INTRODUCTION

Core accretion planet formation theories predict that only terrestrial and icy planets can form around very low mass (VLM) stars ($\lesssim 0.1\text{--}0.2 M_{\odot}$), and the formation of gas giant planets is essentially prohibited (e.g., Liu et al. 2019, 2020; Matsumoto et al. 2020; Miguel et al. 2020). The reasons are multifold. First, a low stellar mass results in longer dynamical timescale and longer growth timescale of dust, delaying the formation of planetary cores. Secondly, the mass of dust in protoplanetary disks, the building blocks of planets, is correlated with stellar mass (e.g., Ansdell et al. 2017). A low dust mass in disks around VLM stars leads to low mass of protoplanets, suppressing pebble accretion (Ormel & Liu 2018) and preventing cores from ever reaching the critical mass to trigger runaway gas accretion. Last but not least, observed stellar accretion rates suggest that disks around VLM stars evolve faster than those around higher mass stars, further daunting the task of planet formation (Manara et al. 2012; Liu et al. 2020). In addition, water snowline has been proposed to be the preferred site of planetesimal and planet formation due to its enhanced local dust-to-gas ratio (Ormel 2017). Around VLM stars, snowline is close to the star at $r \sim 0.1$ au. Therefore compact systems with rocky planets like the TRAPPIST-1 (Gillon et al. 2016) are expected, while planet formation at $r \gtrsim 1$ au is not (Miguel et al. 2020).

Indeed, statistical studies show that at small orbital separations rocky and icy planets are common around M dwarfs (e.g., Dressing & Charbonneau 2015), while the occurrence rate of gas giant planets dives from 14% around $2 M_{\odot}$ stars to 3% around $0.5 M_{\odot}$ stars (Johnson et al. 2010). Around VLM stars, only a handful of gas giant planets have

ever been found (e.g., GJ 3512; Morales et al. 2019), and their formation mechanism is a mystery. Since their host stars are mature main sequence stars that have finished planet formation long before, it is unclear where and when do those planets form. Protoplanetary disks around VLM stars serve as excellent laboratories for investigating planet formation in these extreme environments.

The Atacama Large Millimeter/submillimeter Array (ALMA) has revealed a variety of sub-structures in protoplanetary disks, such as rings, gaps, cavities, spirals, and crescent structures. While rings/gaps are the most common (e.g., Andrews et al. 2018; Long et al. 2018; Cieza et al. 2020), roughly 10 disks show azimuthal asymmetries (e.g., Francis & van der Marel 2020; van der Marel et al. 2020; Tsukagoshi et al. 2019; Pérez et al. 2018; Dong et al. 2018b; Cieza et al. 2017). Disks around VLM stars also harbor rings and gaps (e.g., Kurtovic et al. 2020); however, azimuthal asymmetries have not yet been reported. Asymmetric dust crescents may be local dust traps at gas pressure maxima (e.g., Raettig et al. 2015; Ragusa et al. 2017), thus ideal locations of planet formation (e.g., Chang & Oishi 2010). Three possible origins of asymmetries have been discussed by van der Marel et al. (2020): (a) long-lived anticyclonic vortices at gap edges, possibly opened by companions (e.g., Raettig et al. 2015), (b) gas horseshoes at the edge of eccentric cavities curved by massive companions (e.g., Ragusa et al. 2017), and (c) part of spiral arms (van der Marel et al. 2016) triggered by companions. The main difference between the former two is in the mass of the companions: a vortex can be produced at the edges of gaps opened by planets as low mass as super-Earths (Dong et al. 2018a), whereas a horseshoe needs to be triggered by a much more massive companion, i.e., a brown dwarf. Overall, all three mechanisms suggest the presence of companions (planets) inside the cavity or gap.

In this paper, we report a ring and an asymmetric structure around the VLM star ZZ Tau IRS (spectral type: M4.5 to M5, T_{eff} : 3015 to 3125 K, L_{star} : 0.02 to 0.13 L_{\odot} , M_{*} : 0.09 to 0.16 M_{\odot} , White & Hillenbrand 2004; Andrews et al. 2013; Herczeg & Hillenbrand 2014) in the Taurus star forming region at an assumed distance of 130.7 pc¹ taken from Akeson et al. (2019). The stellar luminosity is 0.017 to 0.113 L_{\odot} (White & Hillenbrand 2004; Andrews et al. 2013; Herczeg & Hillenbrand 2014, scaled by the updated distance), with the large uncertainty mainly due to factors including flux calibration and extinction (see the discussions in Herczeg & Hillenbrand 2014). With these T_{eff} and L_{star} , the Baraffe et al. (2015) isochrone yields a stellar mass around 0.1 M_{\odot} at an age of 1 to 12 Myr consistently. ZZ Tau IRS is a single star (i.e., not identified as a spectroscopic binary; Kounkel et al. 2019) while its companion ZZ Tau is 35'' away. Its spectral energy distribution (SED; Figure 5 in Appendix A) does not show any deficits at IR wavelengths $\lambda \lesssim 10 \mu\text{m}$, and thus ZZ Tau IRS was not classified as having a cavity/gap structure in its disk. The large IR excess relative to the stellar flux in the SED (Figure 5) was interpreted as an edge-on disk (Furlan et al. 2011), and high-resolution optical spectroscopy of ZZ Tau IRS also suggested the existence of a close to edge-on disk based on its narrow emission lines from the optical jet (White & Hillenbrand 2004). The total disk mass (gas + dust) was estimated to be 0.014 M_{\odot} by observations at millimeter wavelengths using the Submillimeter Array (Andrews et al. 2013; Akeson et al. 2019).

2. ALMA ARCHIVE DATA

We used the ALMA archive data at band 7 (program ID: 2016.1.01511.S, PI: J. Patience), summarized in Table 1. The data were calibrated by the Common Astronomy Software Applications (CASA) package (McMullin et al. 2007), following the calibration scripts provided by ALMA. We performed a self-calibration of the visibilities. The phases were self-calibrated once, with fairly long solution intervals (solint = ‘inf’) that combined all spectral windows. To facilitate analyses later (§ 4), we shifted the observed dust continuum images to minimize the asymmetry relative to the phase center using the procedure described in Appendix B.

The final synthesized dust continuum image of the combined data is shown in Figure 1. In the CLEAN task, we set the uv -taper ($0.4 \times 500.0 \text{ M}\lambda$ at PA of 48°) with a robust parameter of -2.0 to obtain a nearly circular beam, and we did not use the ‘multi-scale’ option. The r.m.s. noise in the region far from the source is 268 $\mu\text{Jy}/\text{beam}$ with a beam size of $254 \times 248 \text{ mas}$ at a position angle (PA) of -61.7° .

The $^{12}\text{CO } J = 3 \rightarrow 2$ line data (Table 1) were extracted by subtracting the continuum in the uv plane using the `uvcontsub` task in the CASA tools. A line image cube with a channel width of 0.5 km/s was produced by the CLEAN task. The integrated line flux map (moment 0) and the intensity-weighted velocity map (moment 1) are shown in Figure 2. The channel maps at $+1.0$ to $+13.0 \text{ km/s}$ are shown in Figure 7 in the Appendix C. The r.m.s. noise in the moment 0 map is 61.4 mJy/beam-km/s with a beam size of $283 \times 156 \text{ mas}$ at a PA of -50.2° , and the r.m.s. noise

¹ We do not use the GAIA distance of 105.7 pc because the astrometric solution is poor with a value of the renormalized unit weight error (RUWE) of 2.490 (GAIA EDR3; Gaia Collaboration et al. 2020).

Table 1. ALMA observations and imaging parameters

Observations				
Observing date (UT)	2017.Jul.6			
Project code	2016.1.01511.S (PI: J. Patience)			
Time on source (min)	4.5			
Number of antennas	42			
Baseline lengths	16.7 m to 2.6 km			
Baseband Freqs. (GHz)	331.9 (cont.)	333.8 (cont.)	343.9 (cont.)	345.8 ($^{12}\text{CO } J = 3 \rightarrow 2$)
Channel width (MHz)	15.6	15.6	15.6	0.488
Continuum band width (GHz)	7.5			
Bandpass calibrator	J0510+1800			
Flux calibrator	J0510+1800			
Phase calibrator	J0438+3004			
Typical PWV (mm)	0.60			
Imaging	Dust continuum		$^{12}\text{CO } J = 3 \rightarrow 2$	
Robust clean parameter	-2.0		2.0	
Outer uv -taper parameter	$0.4 \times 500.0 \text{ M}\lambda$ with 48.0°		...	
Beam shape	$254 \times 248 \text{ mas}$ at PA of -61.7°		$283 \times 156 \text{ mas}$ at PA of -50.2°	
r.m.s. noise (mJy/beam)	0.268		9.56 at 0.5 km/s bin	

in the moment 1 map is 9.56 mJy/beam at 0.5 km/s bin. The peak signal-to-noise ratio (SNR) is 24.1 in the channel map of +4.0 km/s.

3. RESULTS

3.1. Dust continuum emission

Figure 1 shows dust continuum images of the ZZ Tau IRS disk in band 7, as well as its radial and azimuthal profiles. We found two structures: a ring at $r \sim 50$ au (hereafter we refer to the ZZ Tau IRS disk as a ‘ring’) in Figure 1(b) and an azimuthal asymmetry with a contrast ratio of 1.39 ± 0.05 between its peak and the opposite side on the ring in Figure 1(c). The peak SNR in the ring is 78.4. The dust continuum image synthesized with only the imaginary part (which efficiently detects asymmetric structures) indicates that the asymmetric structure in the ring is significant with a peak SNR of 34.3 in the central panel in Figure 6 in the Appendix B. In the azimuthal profile (Figure 1c), we found two peaks at PAs of $\sim 130^\circ$ and $\sim 310^\circ$. Such a two-peak structure along a disk major axis is commonly found in low spatial resolution images of rings ($\sim 0''.2\text{--}0''.4$; e.g., Ansdell et al. 2016). Our visibility analyses in § 4 suggest that the peak at a PA of $\sim 310^\circ$ is caused by beam effects. Hereafter we refer to the peak at a PA of $\sim 130^\circ$ as the asymmetry.

The total flux density of the dust continuum derived from visibility analyses in § 4 is 273.9 ± 27.4 mJy (Table 2), assuming a 10 % uncertainty in the absolute flux calibration, consistent with previous single-disk observations (300 ± 40 mJy, Di Francesco et al. 2008). The peak brightness temperature in the ring calculated from the best-fit model in the visibility analyses (§ 4) is 14.9 ± 0.9 K assuming a 10 % uncertainty in the absolute flux calibration.

We now estimate the physical properties of the dust ring. The optical depth τ_ν is calculated as:

$$I_\nu = B_\nu(T_{\text{mid}})\{1 - \exp(-\tau_\nu)\}, \quad (1)$$

where I_ν , B_ν , and T_{mid} are the intensity, the Planck function, and the midplane temperature, respectively. We use the midplane temperature profile with a simplified expression for a passively heated, flared disk in radiative equilibrium (e.g., Dullemond et al. 2001):

$$T_{\text{mid}}(r) = \left(\frac{\phi L_*}{8\pi r^2 \sigma_{\text{SB}}} \right)^{0.25}, \quad (2)$$

where L_* is the stellar luminosity (0.017 to 0.113 L_\odot), ϕ is the flaring angle, and σ_{SB} is the Stefan–Boltzmann constant. If the starlight-absorbing small dust grains (sub-micron-sized) have a similar spatial distribution to the large dust grains

(millimeter-sized) traced by millimeter emission (similar to the PDS 70 disk; Hashimoto et al. 2012; Keppler et al. 2019), the inner wall of the ring is directly exposed to stellar radiation, and ϕ reaches unity. In this case, at $r = 45$ au where the asymmetry is located (see visibility analyses in § 4), Equation (2) yields $T_{\text{mid}} = 17.8\text{--}28.6$ K (uncertainty due to the stellar luminosity). The corresponding optical depth τ_ν is 0.5–1.4 based on Equation (1). Therefore, the asymmetry is marginally optically thin. The rest of the ring is expected to be optically thinner. Approximating the entire disk as an optically thin structure, the total flux corresponds to a total mass (gas + dust) of 7.6–15.7 M_{Jup} assuming the dust temperature of $T_{\text{mid}} = 17.8\text{--}28.6$ K, an opacity per unit dust mass of $\kappa_\nu = 3.45$ cm² g⁻¹ at 345 GHz (Beckwith & Sargent 1991), and a gas-to-dust mass ratio of 100. We note that the dust mass estimate is a lower limit since the actual dust temperature can be lower. The large dust grains are expected to concentrate at the pressure peak outside the cavity wall and reach a temperature lower than that estimated using Equation 2 with $\phi \sim$ unity. In the extreme case, the observed cavity in large dust grains may even be filled with small dust grains (e.g., “missing cavities”; Dong et al. 2012), resulting in substantially lower temperature at the ALMA ring location.

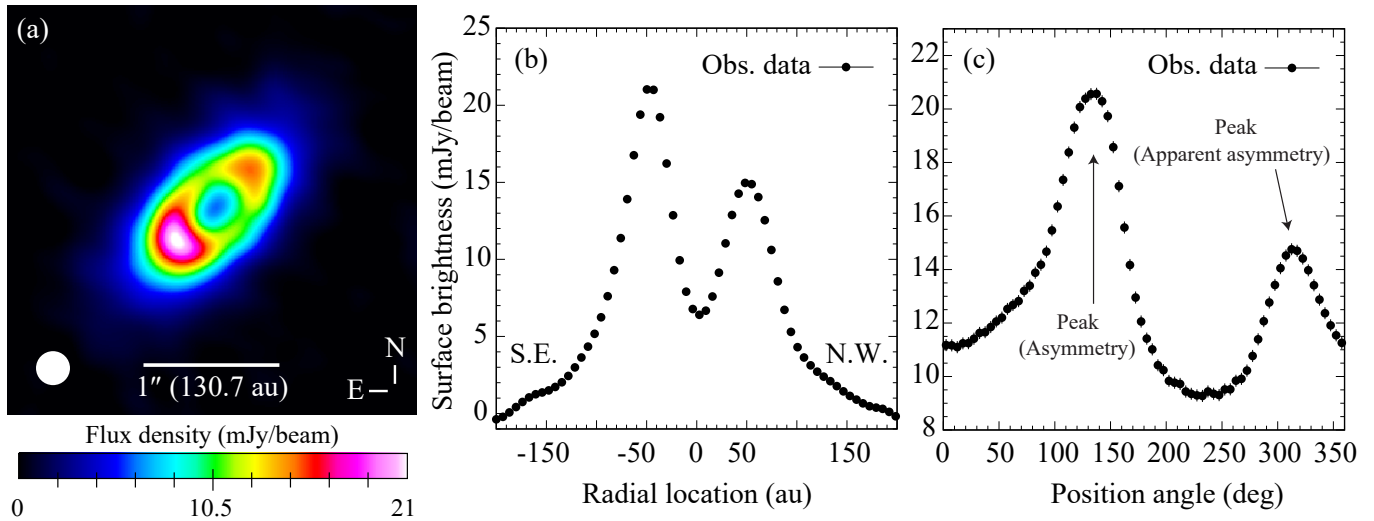


Figure 1. Synthesized image of the dust continuum for the ZZ Tau IRS ring obtained from band 7. (a) Entire image. The r.m.s. noise measured in the region far from the object is 0.268 mJy/beam with a beam size of 254×248 mas at a PA of -61.7° . (b) Radial cut along the disk major axis at a PA of 135° in panel (a). (c) Azimuthal profile along the elliptical ring in panel (a). Two peaks are found at PAs of $\sim 130^\circ$ and $\sim 310^\circ$. Only the peak at a PA of $\sim 130^\circ$ is a real asymmetry, whereas that at PA of $\sim 310^\circ$ is an apparent structure due to a low spatial resolution effect (see § 4).

3.2. Gas emission

The integrated line flux map of $^{12}\text{CO } J = 3 \rightarrow 2$ in Figure 2(a) shows a single-peak structure with a peak flux of 1.0 ± 0.1 Jy/beam·km/s at 16.3σ and a total flux above 3σ of 1.9 ± 0.19 Jy·km/s assuming a 10 % uncertainty in the absolute flux calibration. As shown in the channel maps in Figure 7 in the Appendix C, the ^{12}CO emission is absorbed at 6.5–7.0 km/s, and thus the total flux could be a lower limit. The brightness temperature map of ^{12}CO converted from the moment 8 map (maximum values of the spectrum) is shown in Figure 2(b). Since $^{12}\text{CO } J = 3 \rightarrow 2$ could be generally optically thick, it could be a good tracer for the gas temperature in the emitting region. At the location of the asymmetry, the brightness temperature of ^{12}CO is ~ 35 K, higher than the 17.8–28.6 K estimated by Equation (2). This could be because the emitting surface of ^{12}CO is in the upper hotter layer of the disk. Figure 2(d) shows the ^{12}CO position–velocity (PV) diagram (channel maps: Figure 7 in the Appendix C) along PA = 135° . We overplotted the loci of the peak emission of a Keplerian disk with an inclination of 60° (see § 4) around a central star with masses of 0.1, 0.2, and 0.3 M_\odot , and found that the dynamical mass of ZZ Tau IRS is $\sim 0.1\text{--}0.3 M_\odot$. This value is consistent with the spectroscopically determined mass (0.1–0.2 M_\odot ; Andrews et al. 2013; Herczeg & Hillenbrand 2014). Note that we assume that the systemic velocity of ZZ Tau IRS is 6.5 km/s in the PV diagram.

4. VISIBILITY ANALYSES

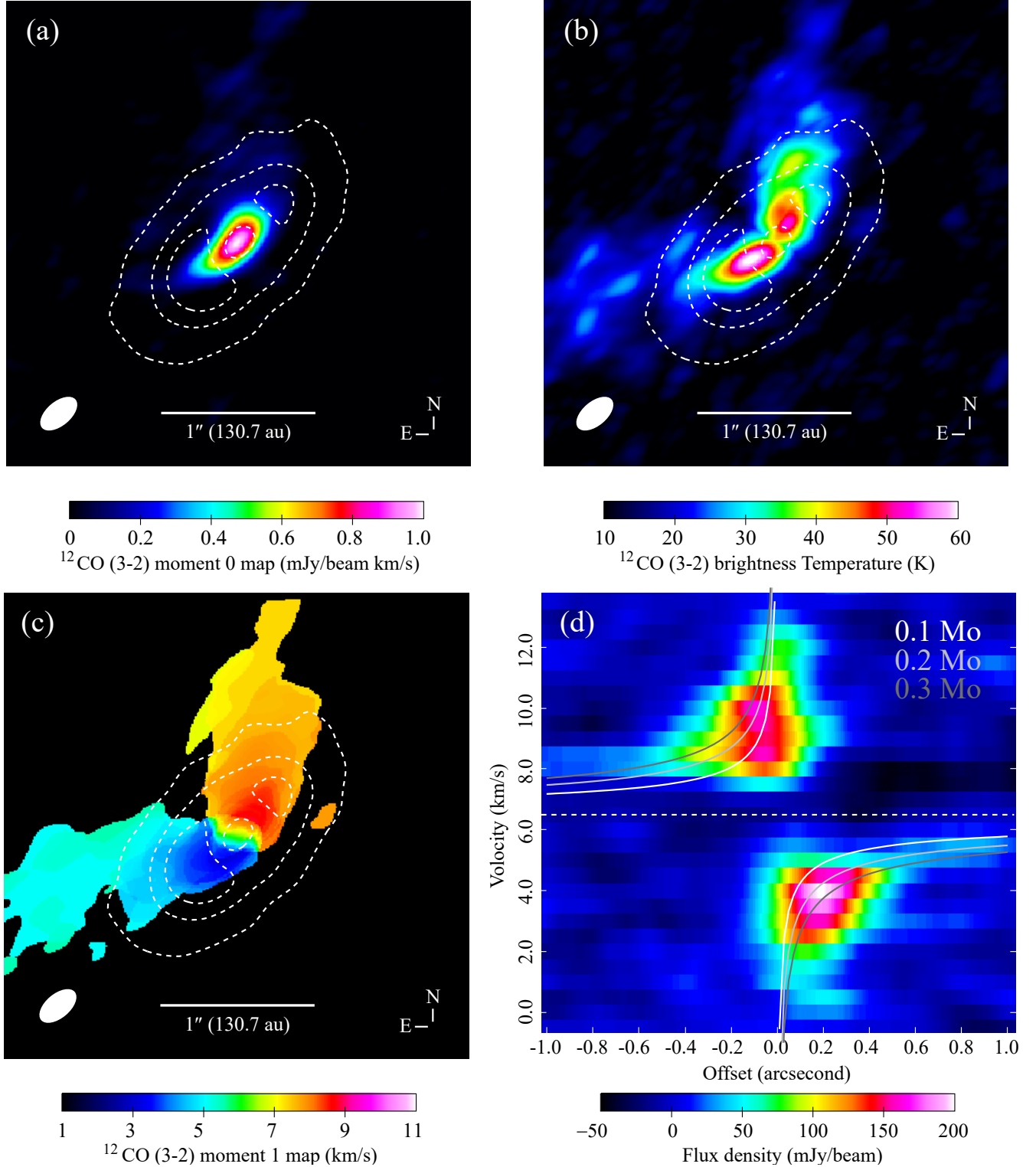


Figure 2. Synthesized images of the ^{12}CO $J = 3 \rightarrow 2$ emission line for the ZZ Tau IRS ring. (a) ^{12}CO moment 0 map. The r.m.s. noise is 61.4 mJy/beam-km/s with a beam size of 283×156 mas at a PA of -50.2° . (b) ^{12}CO moment 8 map converted to the brightness temperature. (c) ^{12}CO moment 1 map. The r.m.s. noise is 9.56 mJy/beam at 0.5 km/s bin. The dotted contours represent the dust continuum at 10, 30, and 50 σ . (d) PV diagram along a PA of 135° taken from § 4. The three lines denote loci of the peak emission of a Keplerian disk with a disk inclination of 60° around 0.1 to 0.3 M_\odot stars at $d = 130.7$ pc. The systemic velocity (white dotted line) is assumed to be 6.5 km/s.

Since the contrast of the asymmetry in the ZZ Tau IRS ring is of order unity, an imaging artifact such as a sidelobe of the bright ring could generate an apparent asymmetry. To characterize the disk structure, we performed forward modelling in which the observed visibilities are reproduced with a parametric model of the ring in the visibility domain.

The ZZ Tau IRS disk is assumed to consist of a ring and an asymmetry. The model ring consists of a narrow Gaussian ring (ring A) superposed on a wide Gaussian ring (ring B) as shown in Figure 3(a), and is described as follows:

$$I_{\text{ring}}(r) \propto \exp\left(-\frac{(r - r_{\text{peak,ringA}})^2}{2\sigma_{r,\text{ringA}}^2}\right) + \delta \exp\left(-\frac{(r - r_{\text{peak,ringB}})^2}{2\sigma_{r,\text{ringB}}^2}\right), \quad (3)$$

where $r_{\text{peak,ringA}}$, $\sigma_{r,\text{ringA}}$, $r_{\text{peak,ringB}}$, $\sigma_{r,\text{ringB}}$, and δ are the radial peak positions and standard deviations of two Gaussian rings and a scaling factor between the two, respectively. The width of the ring (FWHM) is calculated as $2.355\sigma_{\text{ring}}$.

The asymmetry is defined as an elliptical Gaussian function in polar coordinates as follows:

$$I_{\text{asym}}(r, \theta) \propto \exp\left(-\frac{(r - r_{\text{peak,asym}})^2}{2\sigma_{r,\text{asym}}^2} - \frac{(\theta - \theta_{\text{peak,asym}})^2}{2\sigma_{\theta,\text{asym}}^2}\right), \quad (4)$$

where $r_{\text{peak,asym}}$, $\theta_{\text{peak,asym}}$, $\sigma_{r,\text{asym}}$, and $\sigma_{\theta,\text{asym}}$ are the radial peak position, azimuthal peak position, radial standard deviation, and azimuthal standard deviation, respectively. The flux for the asymmetry is normalized to F_{asym} . The combined model image is magnified and rotated with an inclination (i) and a PA. The total flux for the combined model image is normalized to F_{total} . The radial and azimuthal widths (FWHM) of the asymmetry are $2.355\sigma_{r,\text{asym}}$ and $2.355\sigma_{\theta,\text{asym}}$, respectively. In total, there are 13 free parameters in our model (F_{total} , F_{asym} , $r_{\text{peak,ringA}}$, $\sigma_{r,\text{ringA}}$, $r_{\text{peak,ringB}}$, $\sigma_{r,\text{ringB}}$, δ , $r_{\text{peak,asym}}$, $\theta_{\text{peak,asym}}$, $\sigma_{r,\text{asym}}$, $\sigma_{\theta,\text{asym}}$, i , PA).

The model image was converted to complex visibilities with the public Python code `vis_sample` (Loomis et al. 2017), in which model visibilities are samples with the same (u , v) grid points as the observations. The model visibilities are deprojected² with the system PA and i as free parameters. The fitting is performed with a Markov chain Monte Carlo (MCMC) method in the `emcee` package (Foreman-Mackey et al. 2013). The log-likelihood function $\ln L$ in visibility analyses is

$$\ln L = -0.5 \sum [W_j \{(\text{Re}V_j^{\text{obs}} - \text{Re}V_j^{\text{model}})^2 + (\text{Im}V_j^{\text{obs}} - \text{Im}V_j^{\text{model}})^2\}], \quad (5)$$

where the subscript j represents the j -th data. V_j^{obs} , V_j^{model} , and W_j are observed and model visibilities and weights corresponding to $1/\sigma_j^2$ (σ_j is the rms noise of a given visibility. See details in CASA Guides³), respectively. The values of V_j^{obs} and W_j (i.e., $1/\sigma_j^2$) are provided in the measurement set of ALMA data. Our calculations used flat priors with the parameter ranges summarized in Table 2. We ran 3,000 steps with 100 walkers, and discarded the initial 1,000 steps as the burn-in phase based on trace plots in Figure 8 in Appendix D.

The fitting results with uncertainties computed from the 16th and 84th percentiles, the radial profile of best-fit surface brightness for the ring with a raw resolution, the best-fit model image, and the probability distributions for the MCMC posteriors are shown in Table 2, Figure 3(a), Figure 3(d), and Figure 9 in the Appendix E, respectively. We subtracted modeled visibilities from observed visibilities (Figure 10 in Appendix F), and made a CLEANed image (Figure 3e) in which we did not find significant residuals. To calculate the value of the reduced- χ^2 , we derived a factor between the weights and standard deviations (referred to as `stddev`) in the visibilities by calculating the standard deviations of the real and imaginary parts in 2 $k\lambda$ bins along the azimuthal direction in the visibility domain. The values of weights W_j are provided in the measurement set of ALMA data while the standard deviations (`stddev`) are calculated in our fitting. The visibilities were deprojected with $i = 60^\circ$ and PA = 135° . Figure 11 in Appendix G shows a comparison between the weights and standard deviations (`stddev`⁻²). We found that the weights are typically $4.0\times$ higher than the standard deviations. Finally, we calculated a reduced- χ^2 of 1.91. We also conducted visibility analyses using a model with one Gaussian ring + one asymmetry (i.e., $\delta = 0$), and found significant residuals. Thus, the model with two Gaussian rings + one asymmetry is necessary to reproduce the observed dust continuum image.

² Visibilities are deprojected in the uv -plane using the following equations (e.g., Zhang et al. 2016): $u' = (u \cos \text{PA} - v \sin \text{PA}) \times \cos i$, $v' = (u \sin \text{PA} + v \cos \text{PA}) \times \cos i$, where i and PA are free parameters in our visibility analyses in § 4.

³ <https://casaguides.nrao.edu/index.php/DataWeightsAndCombination>

Table 2. Results of visibility analyses and parameter ranges

$r_{\text{peak,ringA}}$	$\text{FWHM}_{\text{ringA}}$	$r_{\text{peak,ringB}}$	$\text{FWHM}_{\text{ringB}}$	δ	i	PA
(au)	(au)	(au)	(au)		(deg)	(deg)
(1)	(2)	(3)	(4)	(5)	(6)	(7)
$57.51^{+0.19}_{-0.18}$	$41.08^{+0.63}_{-0.60}$	$83.62^{+1.61}_{-1.67}$	$133.65^{+1.59}_{-1.62}$	$0.34^{+0.01}_{-0.01}$	$60.16^{+0.07}_{-0.07}$	$134.73^{+0.09}_{-0.09}$
{0.0 .. 117.6}	{0.0 .. 78.4}	{0.0 .. 117.6}	{78.4 .. 196.1}	{0.0 .. 1.0}	{50.0 .. 70.0}	{125.0 .. 145.0}

F_{total}	F_{asym}	$r_{\text{peak,asym}}$	$\theta_{\text{peak,asym}}$	$\text{FWHM}_{r,\text{asym}}$	$\text{FWHM}_{\theta,\text{asym}}$
(mJy)	(mJy)	(au)	(deg)	(au)	(deg)
(8)	(9)	(10)	(11)	(12)	(13)
$273.94^{+0.66}_{-0.67}$	$14.51^{+0.25}_{-0.24}$	$45.15^{+0.22}_{-0.21}$	$-18.17^{+0.52}_{-0.52}$	$11.31^{+0.98}_{-1.01}$	$103.07^{+1.59}_{-1.60}$
{250.0 .. 300.0}	{0.0 .. 100.0}	{0.0 .. 117.6}	{-45.0 .. +45.0}	{0.0 .. 117.6}	{0.0 .. 360.0}

NOTE— Parentheses describe parameter ranges in our MCMC calculations.

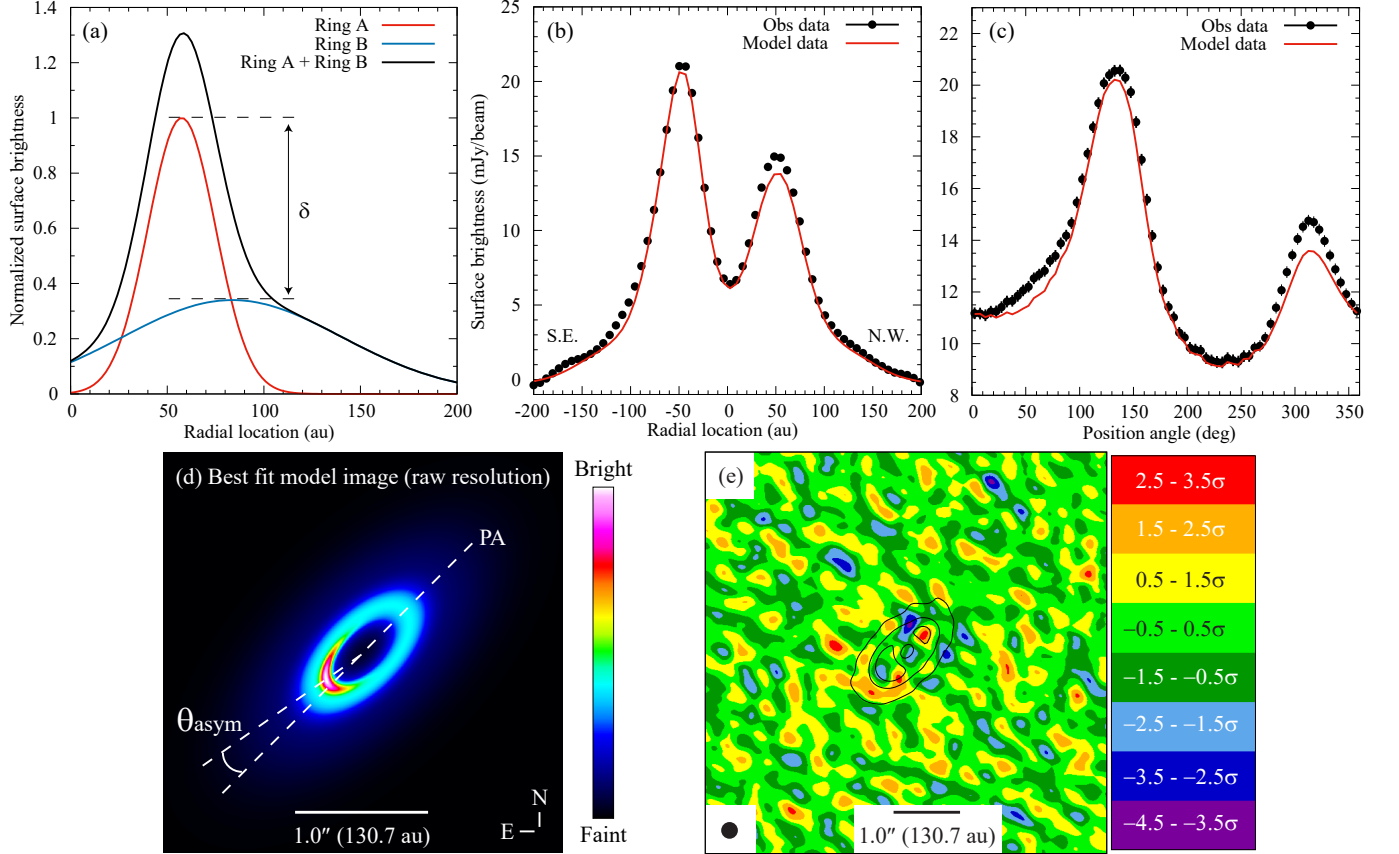


Figure 3. (a) Azimuthally averaged radial surface brightness for the best-fit model with a raw resolution. The asymmetry is not included in this panel. (b and c) Radial and azimuthal profiles of the observations and the best-fit model convolved with the beam in observations of 254×248 mas at a PA of -61.7° . Observed data are same with those in Figure 1(b) and (c). (d) Best-fit model image ($3'' \times 3''$). (e) Residual image ($6'' \times 6''$). The reduced- χ^2 is 1.91. The black dotted contours represent the dust continuum image at 10, 30, and 50 σ .

Though the observed dust continuum image in Figure 1(a) shows two peaks along the ring major axis, our visibility analyses suggest that only the one at PA = 130° is real.

The radial ring position (i.e., the peak position) and its FWHM (Ring A + Ring B) in the model image were measured to be 58 and 49 au in Figure 3(a). The contrast in the asymmetry, which is the ratio between the peak brightness at the asymmetry and that at its opposite side on the ring, is measured to be 3.0 in Figure 3(d).

5. DISCUSSION

5.1. Azimuthal asymmetry

Azimuthal asymmetries in rings have been identified in roughly ten protoplanetary disks (e.g., van der Marel et al. 2020). At band 7, their shape parameters (e.g., the radial FWHM and the aspect ratio defined as the azimuthal FWHM divided by the radial FWHM) are summarized in Table 3⁴. All but ZZ Tau IRS are intermediate mass stars ($\sim 2 M_{\odot}$). In Figure 4 we compare various properties of these asymmetries as a function of the peak radial location. Though ZZ Tau IRS is a VLM star, its asymmetry has similar properties to other asymmetries around more massive stars, implying a similar origin.

We explore the correlation in Figure 4 by calculating Pearson’s correlation coefficient r for logarithmic numbers except the aspect ratio. The 5% significance values for Pearson’s r with $n = 7$ and 8 are 0.75 and 0.71, respectively (Pugh & Winslow 1966). We found two (marginally) statistically significant relations: radial location *v.s.* radial FWHM ($r = 0.89$), and radial location *v.s.* azimuthal FWHM ($r = 0.69$; top panels in Figure 4). Asymmetric structures have been interpreted as dust traps at pressure maxima in gas vortices (e.g., Raettig et al. 2015) or horseshoes (e.g., Ragusa et al. 2017). The radial width of a gas pressure bump is expected to be comparable to the gas scale height (e.g., Dullemond et al. 2018), typically prescribed as $H(r) \propto r^q$ with $q \sim$ unity (e.g., assuming $T(r) \propto r^{-0.5}$, $q = 1.25$). The most significant correlation we see in Figure 4, radial location *v.s.* radial FWHM, may simply trace the dependence of the radial size of gas pressure structure on r .

Another interpretation of asymmetries is that they are part of spiral arms induced by companions (e.g., van der Marel et al. 2016). One way to distinguish these mechanisms is to derive the spectral index from multi-wavelength observations, which may constrain the size of the dust grains (e.g., Testi et al. 2014). Dust trapping in gas vortices and horseshoes results in a bigger dust size, while spiral arms are not expected to trap dust particles as they differentially rotate with respect to the local disk material (Papaloizou et al. 2007; Li et al. 2020). Measuring the pattern speed of asymmetries may also shed light on their origin, as vortices and horseshoes are expected to move at the local Keplerian velocity while spirals corotate with their drivers.

5.2. Gravitational stability

ZZ Tau IRS’ disk is one of the most massive among VLM stars (cf., Kurtovic et al. 2020). We examine its gravitational stability. Theoretical studies (e.g., Durisen et al. 2007) suggest that if the Toomre (1964) Q -parameter, defined as

$$Q = \frac{c_s \Omega_K}{\pi G \Sigma_{\text{disk}}}, \quad (6)$$

where c_s , Ω_K , and Σ_{disk} are the sound speed, the Keplerian angular velocity, and the disk (gas) surface density, respectively, is of order of unity, the disk may be subject to gravitational instability (GI). With the scale height of $H \sim c_s / \Omega_K$, Toomre’s Q -parameter can be described as $Q \sim H/r \times M_{\text{star}} / M_{\text{disk}}$, where $M_{\text{disk}} = \pi r^2 \Sigma_{\text{disk}}$. Therefore, if the disk’s aspect ratio is $H/r \sim 0.1$, GI occurs in massive disks with $M_{\text{disk}} / M_{\text{star}} \gtrsim 0.1$. The disk-to-star mass ratio is ~ 0.04 – 0.08 in ZZ Tau IRS (§ 3.1), and thus the disk may be globally gravitationally stable. Meanwhile the Q -value at the asymmetry is 1.7–6.2 assuming a local surface density $\Sigma_{\text{disk}} = \cos i \tau_{\nu} / \kappa_{\nu} = 7$ – 20 g/cm^2 ($i = 60^\circ$ and $\tau_{\nu} = 0.5$ – 1.4 , § 3.1), an opacity per unit dust mass of $\kappa_{\nu} = 3.45 \text{ cm}^2 \text{ g}^{-1}$ at 345 GHz (Beckwith & Sargent 1991), a temperature of 17.8–28.6 K (§ 3.1), and a gas-to-dust mass ratio of 100. Hence, the asymmetry may also be marginally stable.

5.3. Possible warped inner disk

ZZ Tau IRS has been suggested to have an edge-on inner disk (White & Hillenbrand 2004; Furlan et al. 2011), because the IR excess is larger than the optical stellar flux due to partial disk obscuration of the star (Figure 5 in

⁴ The physical quantities of other asymmetries are taken from van der Marel et al. (2020). V1247 Ori shows a crescent structure in ALMA band 7 (Kraus et al. 2017). However, we do not include V1247 Ori because the structure does not have a Gaussian profile (Kraus et al. 2017). Though HD 142527 also shows a crescent structure in ALMA band 7 (Fukagawa et al. 2013), the visibility analyses in van der Marel et al. (2020) did not find convergence; thus, we do not include HD 142527.

Table 3. Stellar mass and physical quantities for asymmetries

Object	Stellar mass	Radial location	Radial FWHM	Azimuthal FWHM	Aspect ratio	Contrast	Flux ratio	Refs
	(M_{\odot})	(au)	(au)	(deg; au)			(%)	
(1)	(2)	(3)	(4)	(5)	(6)	(7)	(8)	(9)
ZZ Tau IRS	0.2	45	11.3	103; 80.9	7.2	3.0	5.3	a,a
MWC 758	1.9	50	7.5	49; 42.7	5.7	4.4	6.4	b,c
		90	15	47; 73.8	4.9	11.7	20.0	b,c
HD 34282	2.0	137	110	52; 124.3	1.1	1.7	4.8	b,d
SR 21	2.1	55	19	82; 78.7	4.1	2.1	12.5	b,c
		58	19	165; 166.9	8.8	2.0	26.0	b,c
AB Aur	2.3	170	96	122; 361.8	3.8	2.7	39.5	b,c
IRS 48	2.2	70	29	58; 70.8	2.4	—	—	b,c

NOTE— (1) Object name. MWC 758 and SR 21 have two asymmetries (van der Marel et al. 2020). (2) Stellar mass. (3) Radial location. (4) Radial FWHM calculated by $2.355\sigma_r$. The radial FWHM of the IRS 48 asymmetry is calculated with $2.17\sigma_r$ because the radial profile for IRS 48 was found to be best fit with a 4th power in 2D Gaussian in van der Marel et al. (2020). (5) Azimuthal FWHM. (6) The aspect ratio defined as the azimuthal FWHM divided by the radial FWHM. (7) Contrast measured in the model between the peak brightness and the opposite side of the ring. The model images are constructed with the parameters from the literature in column (9). For SR 21, since the azimuthal positions of the two asymmetries are located at almost opposite sides, the contrast of the each asymmetry was measured for a model containing only one asymmetry and the ring. For IRS 48, the contrast is not measured because the model contains only the asymmetry without the ring (van der Marel et al. 2020). (8) Ratio of the asymmetry to total flux in the model. For IRS 48, this value is not measured because the model contains only the asymmetry without the ring (van der Marel et al. 2020). (9) References for information of stellar masses and properties of asymmetries: a) this work, b) Garufi et al. (2018), c) van der Marel et al. (2020), d) van der Plas et al. (2017).

the Appendix A). Our visibility analyses suggest that the outer ring at $r = 50$ au has an inclination (i) of 60° (§ 4). Radiative transfer calculations for protoplanetary disks (full disks) show that typically the central star starts to be significantly obscured by the disk once the inclination is larger than $\sim 70^\circ$ (e.g., see Figure 2 in Whitney et al. 2013). Hence ZZ Tau IRS could possess an inner disk misaligned with the outer ring. Such warped inner disks have been discovered in twisted gas flow patterns (e.g., Rosenfeld et al. 2014; Mayama et al. 2018) and shadows on the outer disk in NIR scattering images (e.g., Marino et al. 2015). For ZZ Tau IRS, current ALMA gas observations in Figure 2 are insufficient to confirm a twisted gas flow due to low spatial & spectral resolution. Furthermore, high spatial resolution observations of NIR scattering images have not yet been carried out. Another possible explanation of the observed SED is that the source is a “flat spectrum” young stellar object surrounded by an infalling dusty envelope (Calvet et al. 1994). In this case, an extended reflection nebulae around the source is expected in NIR scattered light observations (e.g., similar to T Tau, Whitney & Hartmann 1993). Future observations are necessary to test these hypotheses.

A few possible mechanisms have been proposed to explain warped disks. An exciting one is disk-companion interactions (e.g., Zhu 2019), in which a massive companion with a companion-star mass ratio $q \gtrsim 0.01$ (or $M_p \gtrsim M_J$ around a $0.1M_{\odot}$ star) on an inclined orbit induces both a deep wide gap and a misaligned inner disk. Such a system with a massive companion and a misaligned inner disk has been reported in HD 142527 (Biller et al. 2012; Marino et al. 2015). Future detection of massive companions in the gap would serve as a test for the planet origin hypothesis.

6. CONCLUSION

We analyzed ALMA band 7 archive data (dust continuum and $^{12}\text{CO } J = 3 \rightarrow 2$ emission) of ZZ Tau IRS. The source has been classified as a VLM star with a mass of $\sim 0.1\text{--}0.2 M_{\odot}$ in the literature. The observed $^{12}\text{CO } J = 3 \rightarrow 2$ kinematics suggest a dynamical mass of $\sim 0.1\text{--}0.3 M_{\odot}$, consistent with previous estimates. The ALMA dust continuum image at a spatial resolution of $0''.25$ shows a ring and an asymmetric structures around ZZ Tau IRS. Our visibility analysis confirmed that the observed asymmetry is real rather than apparent.

Our best-fit model of the ALMA dust observations shows that the asymmetry has a radial FWHM of 11.3 au, an aspect ratio of 7.2 (ratio of azimuthal FWHM to radial FWHM), a brightness contrast of 3.0, and the asymmetry contributes 5% of the total disk flux. These metrics are comparable with asymmetries seen around intermediate mass stars ($\sim 2 M_{\odot}$), implying a similar origin, despite ZZ Tau IRS being 10 times less massive. While future high spatial

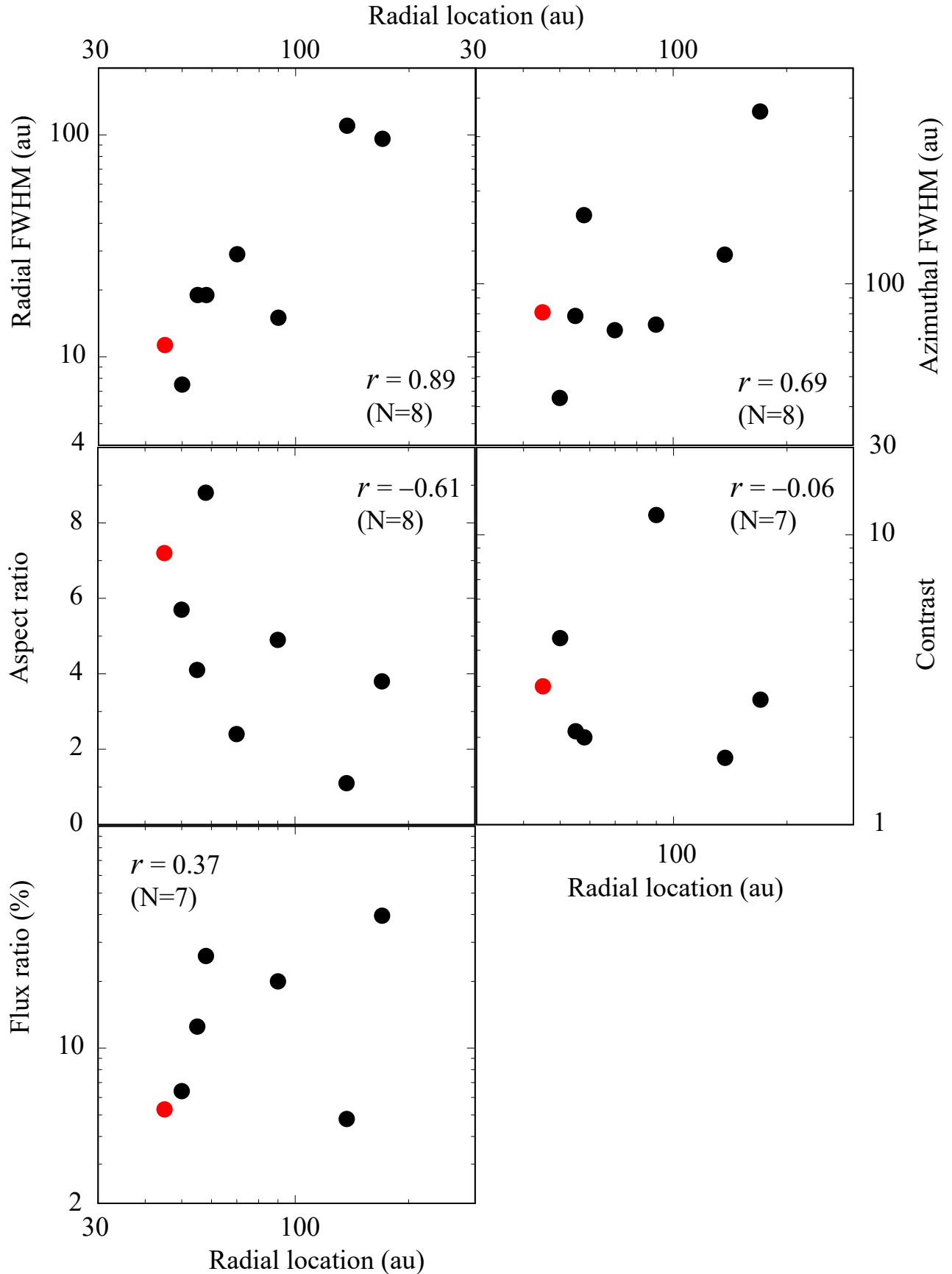


Figure 4. Comparison of the properties of the ZZ Tau IRS asymmetry with other asymmetries around intermediate mass stars as a function of the radial location. The red circle represents ZZ Tau IRS. The physical quantities and their brief explanations are summarized in Table 3. Pearson's correlation coefficient r is inserted in panels. The 5% significance values for Pearson's r with $n = 7$ and 8 are 0.75 and 0.71 , respectively (Pugh & Winslow 1966).

resolution observations in multiple wavelengths with ALMA and JVLA are needed to determine the exact origin of the asymmetry, the three leading hypotheses all invoke companions inside the gap.

The inner disk around ZZ Tau IRS, not visible in our observations, has been inferred to be edge-on based on the SED. Our observations showed that the inclination of the outer disk at $r = 50$ au is 60° . These results imply that the ZZ Tau IRS inner disk may be misaligned relative to the outer ring, and it is possible that the misalignment (and the gap) is produced by a giant planet with $M_p \gtrsim M_J$ on an inclined orbit inside the gap. Future scattered light observations may test this hypothesis by searching for shadows on the outer disk cast by the inner disk.

Overall, the structures found in the ZZ Tau IRS disk suggest the presence of massive companions including gas giant planets at ~ 10 au. This is surprising as the core accretion theories have generally prohibited the formation of such planets around VLM stars (Miguel et al. 2020; Liu et al. 2020, § 1). Hence, ZZ Tau IRS will be a prime target in the investigation of planet formation around VLM stars.

ACKNOWLEDGMENTS

We thank the anonymous referee for a helpful review of the manuscript. We also thank Beibei Liu for discussions. This work was supported by JSPS KAKENHI Grant Numbers 19H00703, 19H05089, and 19K03932, 18H05441, 17H01103. R.D. acknowledges support from the Alfred P. Sloan Foundation and the Natural Sciences and Engineering Research Council of Canada. This paper makes use of the following ALMA data: ADS/JAO.ALMA#2016.1.01511.S. ALMA is a partnership of ESO (representing its member states), NSF (USA), and NINS (Japan), together with NRC (Canada), NSC (Taiwan), ASIAA (Taiwan), and KASI (Republic of Korea), in cooperation with the Republic of Chile. The Joint ALMA Observatory is operated by ESO, AUI/NRAO, and NAOJ. This publication makes use of data products from the Two Micron All Sky Survey, which is a joint project of the University of Massachusetts and the Infrared Processing and Analysis Center/California Institute of Technology, funded by the National Aeronautics and Space Administration and the National Science Foundation. This publication makes use of data products from the Wide-field Infrared Survey Explorer, which is a joint project of the University of California, Los Angeles, and the Jet Propulsion Laboratory/California Institute of Technology, funded by the National Aeronautics and Space Administration.

Software: `vis_sample` (Loomis et al. 2017), `CASA` (McMullin et al. 2007), `emcee` (Foreman-Mackey et al. 2013)

APPENDIX

A. SED OF ZZ TAU IRS

Figure 5 shows the SED of ZZ Tau IRS. Extinction correction is not applied to show the large IR excess relative to the stellar flux. The photometric data without extinction correction are summarized in Table 4.

B. DUST CONTINUUM IMAGES SYNTHESIZED WITH ONLY THE IMAGINARY PART

We shifted the observed dust continuum images to minimize the asymmetry relative to the phase center as follows. First, the proper motions of ZZ Tau IRS were calculated with the function `EPOCH_PROP` in `GAIA ADQL` (Astronomical Data Query Language⁵). The phase centers were corrected to (4h30m51.7346s, +24d41m47.175s) in ICRS using `fixvis` in the `CASA` tools. Next, in order to make the analyses of the disk structure more effective, we further shift the center of the image by searching for the location where the disk asymmetry is minimized. We subtracted the 180° -rotated image in the visibility domain. This procedure corresponds to producing a synthesized image with only the imaginary part of the visibilities. This method has been utilized in the analyses of DM Tau (Hashimoto et al. 2021) and WW Cha (Kanagawa et al. 2021). Since the visibility V is a Fourier transform of the surface brightness distribution of the sky, which is a real quantity, the visibility at $(-u, -v)$ in the uv -plane is a complex conjugate of that at (u, v) ,

$$\bar{V}(u, v) = V(-u, -v). \quad (\text{B1})$$

⁵ <https://gea.esac.esa.int/archive/>

SED of ZZ Tau IRS

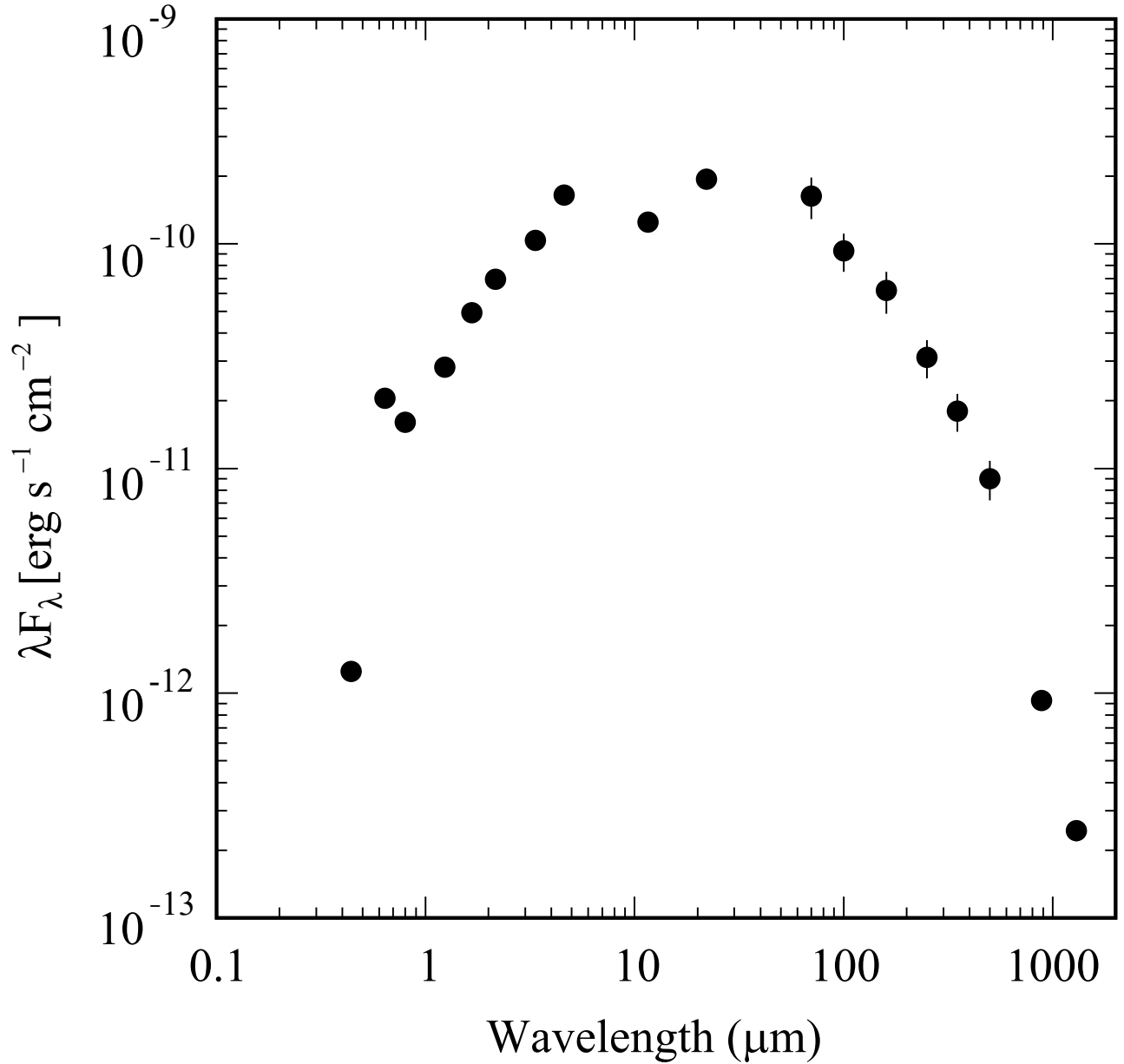


Figure 5. SED of ZZ Tau IRS without extinction correction. The photometric data are summarized in Table 4.

The 180° -rotation of the image with respect to the origin $(x, y) = (0, 0)$ on sky corresponds to flipping the signs of both (x, y) coordinates, i.e., $(x, y) \rightarrow (-x, -y)$. In the visibility domain, this is mathematically equivalent to flipping the signs of (u, v) . Therefore, the visibility of 180° -rotated image is

$$V(u, v) \rightarrow V(-u, -v) = \bar{V}(u, v). \quad (\text{B2})$$

Table 4. Photometric data used in the SED of ZZ Tau IRS

Wavelength	λF_λ	Reference
(μm)	($10^{-12} \text{ erg s}^{-1} \text{ cm}^{-2}$)	
0.44	1.25	USNO-B1.0 (Monet et al. 2003)
0.64	20.5	USNO-B1.0 (Monet et al. 2003)
0.80	16.1	USNO-B1.0 (Monet et al. 2003)
1.23	28.3 ± 0.6	2MASS (Cutri et al. 2003)
1.66	49.2 ± 1.0	2MASS (Cutri et al. 2003)
2.16	69.4 ± 1.5	2MASS (Cutri et al. 2003)
3.35	100.4 ± 2.0	WISE (Cutri & et al. 2014)
4.60	164.5 ± 3.2	WISE (Cutri & et al. 2014)
11.6	124.8 ± 1.6	WISE (Cutri & et al. 2014)
22.1	193.8 ± 2.9	WISE (Cutri & et al. 2014)
70	162.9 ± 34.3	Herschel (Ribas et al. 2017)
100	93.0 ± 18.0	Herschel (Ribas et al. 2017)
160	61.9 ± 13.1	Herschel (Ribas et al. 2017)
250	31.2 ± 6.0	Herschel (Ribas et al. 2017)
350	18.0 ± 3.4	Herschel (Ribas et al. 2017)
500	9.0 ± 1.8	Herschel (Ribas et al. 2017)
885	0.928 ± 0.093	ALMA (this work)
1300	0.244 ± 0.003	SMA (Andrews et al. 2013)

NOTE— Extinction correction is not applied here.

Thus, subtracting the 180° -rotated image is mathematically equivalent to setting the real part to zero and doubling the value of the imaginary part as follows

$$V(u, v) - V(-u, -v) = V(u, v) - \bar{V}(u, v) = 2\text{Im}(u, v). \quad (\text{B3})$$

In other words, the real part contains information on both the symmetric and asymmetric structures of objects, whereas the imaginary part contains only information on the asymmetries. Therefore, by synthesizing the image with only the imaginary part, we selectively remove symmetric structures and reveal only asymmetric structures. We determined the minimum r.m.s. in the central region of the images by shifting the images relative to the new GAIA phase center in the visibility domain by a phase shift of $\exp[2\pi i(u \Delta\text{R.A.} + v \Delta\text{DEC})]$, where u and v are the spatial frequencies and $\Delta\text{R.A.}$ and ΔDEC are the shift values. Figure 6 shows dust continuum images synthesized with only the imaginary part, including the image with the minimum r.m.s. We found shift values for the minimum r.m.s. (ΔRA , ΔDEC) of $(-28 \text{ mas}, -23 \text{ mas})$ relative to the phase center determined by GAIA. The final phase center in the ICRS coordinate is $(4\text{h}30\text{m}51.7325, +24\text{d}41\text{m}47.152)$.

C. $^{12}\text{CO } J = 3 - 2$ CHANNEL MAPS

Figure 7 shows the $^{12}\text{CO } J = 3 - 2$ channel maps at $+1.0$ to $+13.0$ km/s.

D. TRACE PLOTS IN MCMC CALCULATIONS

Figure 8 shows trace plots for 100 walkers for 13 parameters in the model in our visibility analyses (§ 4). The burn-in phase is set as the initial 1,000 steps.

E. HISTOGRAM OF THE MARGINAL DISTRIBUTIONS FOR THE MCMC POSTERiors

Figure 9 shows a corner plot of the MCMC posteriors calculated in visibility analyses in § 4.

F. OBSERVED AND MODELED VISIBILITIES

Figure 10 shows observed and modeled visibilities in our visibility analyses (§ 4).

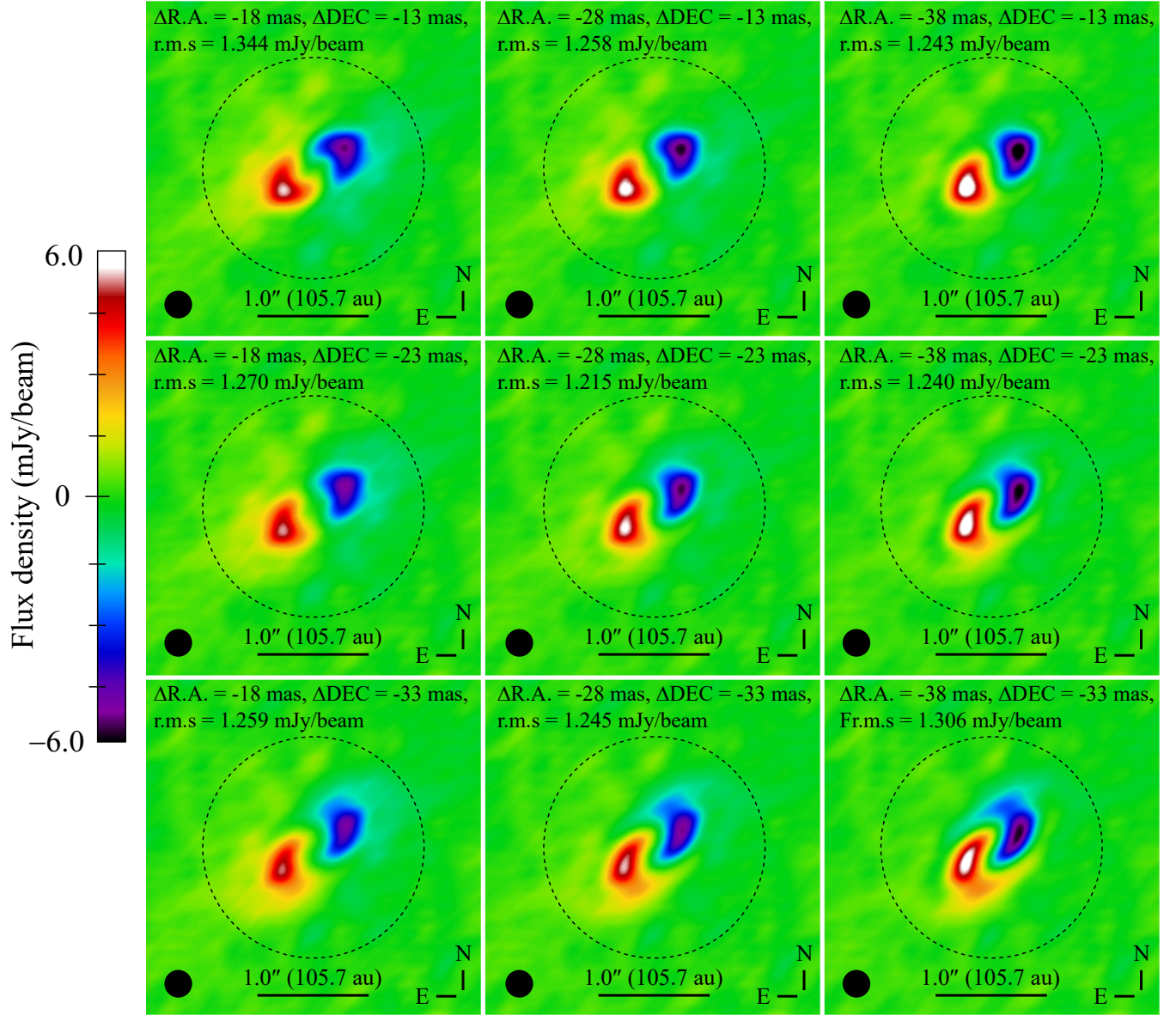


Figure 6. Dust continuum images synthesized with only the imaginary part of the long baseline data by shifting by 10 mas in the R.A. and DEC directions. The r.m.s. value is measured inside the black dotted circle with a diameter of $2''.25$. The $1\text{-}\sigma$ noise is 0.268 mJy/beam measured in a region far from the object. The beam size is 254×248 mas at a PA of -61.7° .

G. WEIGHT VALUES AND STANDARD DEVIATIONS IN THE REAL AND IMAGINARY PARTS

Figure 11 shows a comparison of the values of weights and standard deviations in the real and imaginary parts. The values of weights (W_j) are provided in the measurement set of ALMA data while the standard deviations (stddev) are calculated in each 2 k λ bin in the deprojected visibilities of the real and imaginary parts with $i = 60^\circ$ and PA = 135° . We found that the weights are typically $4.0\times$ higher than $1/\text{stddev}^2$ of the real and imaginary parts at $\sim 100\text{--}600$ k λ .

REFERENCES

- Akeson, R. L., Jensen, E. L. N., Carpenter, J., et al. 2019, *ApJ*, 872, 158, doi: [10.3847/1538-4357/aaff6a](https://doi.org/10.3847/1538-4357/aaff6a)
- Andrews, S. M., Rosenfeld, K. A., Kraus, A. L., & Wilner, D. J. 2013, *ApJ*, 771, 129, doi: [10.1088/0004-637X/771/2/129](https://doi.org/10.1088/0004-637X/771/2/129)

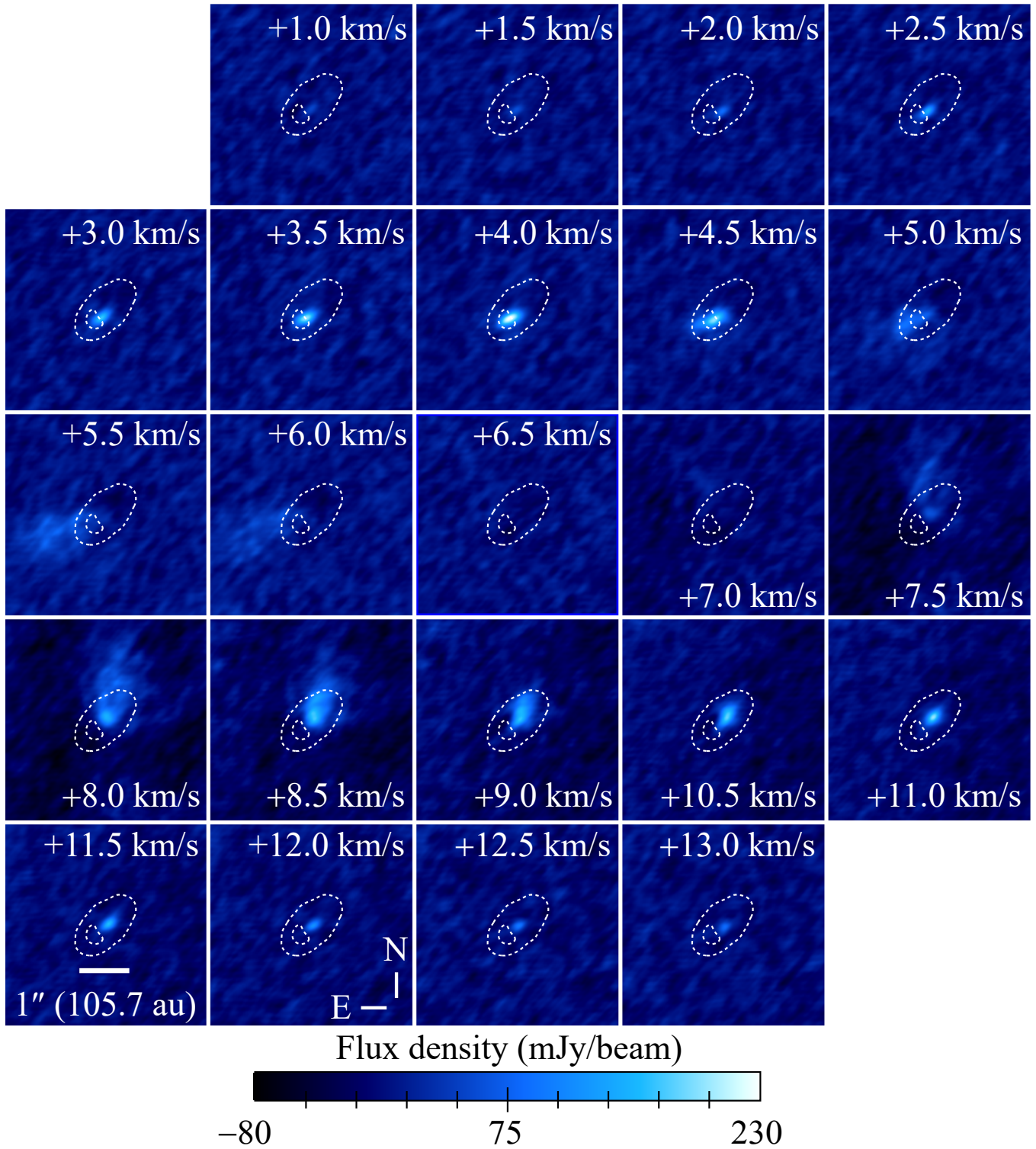


Figure 7. Channel maps of $^{12}\text{CO } J = 3 - 2$. The r.m.s. noise at the 0.5 km/s bin is 9.56 mJy/beam with a beam size of 283×156 mas at a PA of -50.2° .

Andrews, S. M., Huang, J., Pérez, L. M., et al. 2018, ApJL,

Ansdell, M., Williams, J. P., Manara, C. F., et al. 2017, AJ,

869, L41, doi: 10.3847/2041-8213/aaf741

153, 240, doi: 10.3847/1538-3881/aa69c0

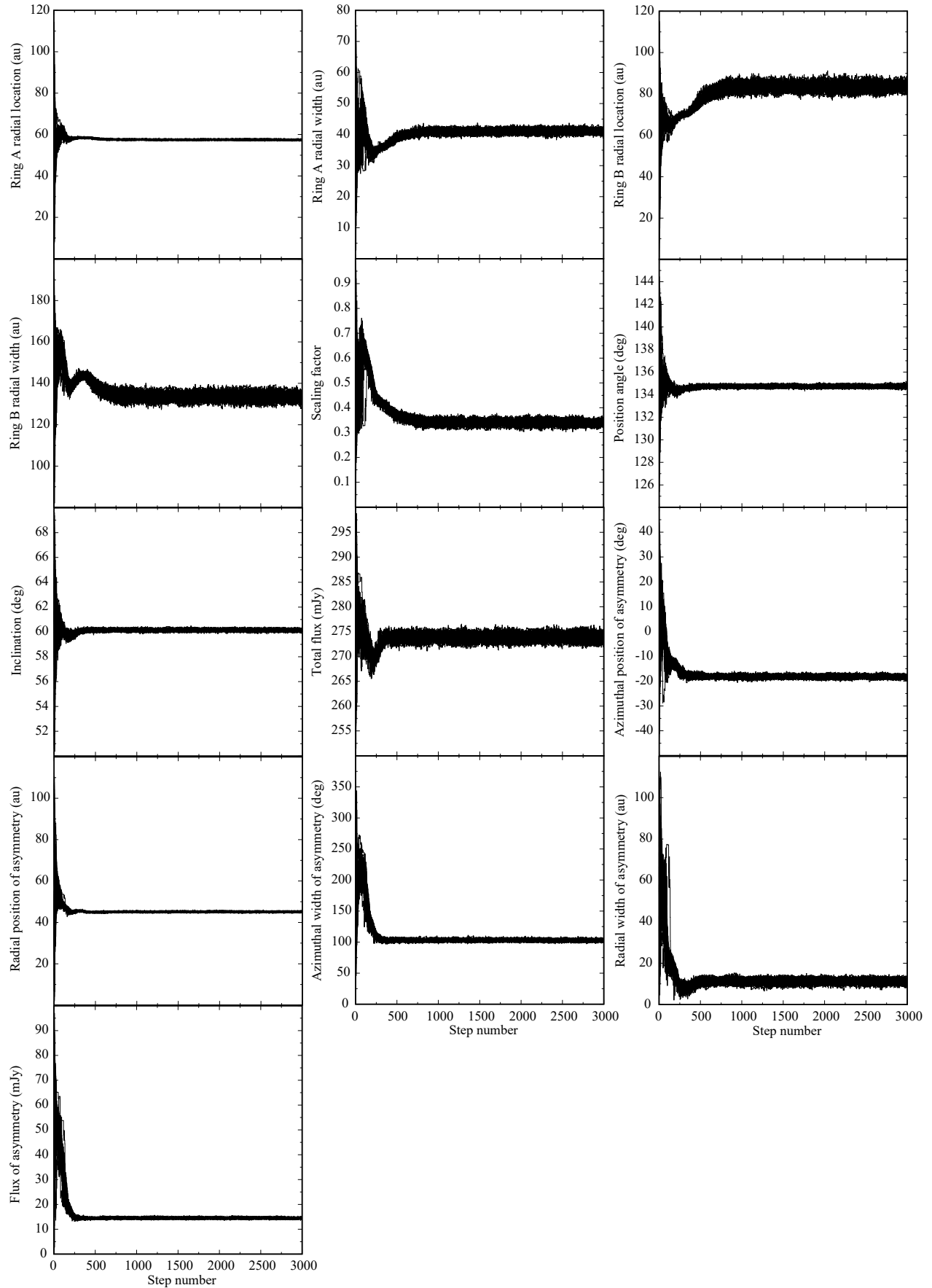


Figure 8. Trace plots for 100 walkers for 13 parameters in the model. The initial 1,000 steps are set as the burn-in phase and are discarded in the histograms of the marginal distributions of the MCMC posteriors in Figure 9.

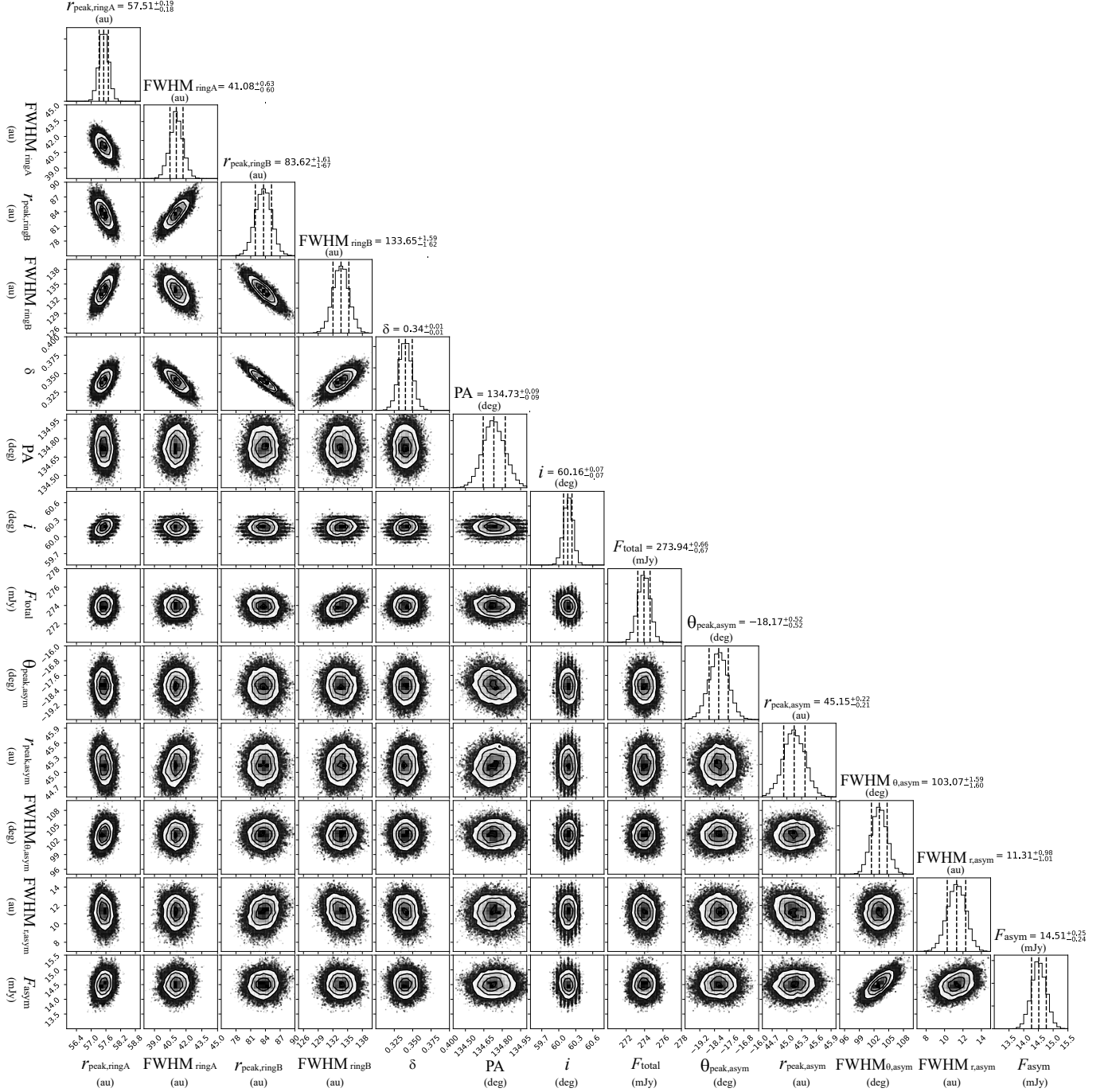


Figure 9. Corner plot of the MCMC posteriors calculated in visibility analyses in § 4. The histograms on the diagonal are marginal distributions of 13 free parameters. The parameter ranges in each parameter are described in Table 2. The vertical dashed lines in the histograms represent the median values and the 1σ confidence intervals for parameters computed from the 16th and 84th percentiles. The off-diagonal plots show the correlation for corresponding pairs of parameters.

Ansdell, M., Williams, J. P., van der Marel, N., et al. 2016, ApJ, 828, 46, doi: [10.3847/0004-637X/828/1/46](https://doi.org/10.3847/0004-637X/828/1/46)

Beckwith, S. V. W., & Sargent, A. I. 1991, ApJ, 381, 250, doi: [10.1086/170646](https://doi.org/10.1086/170646)

Baraffe, I., Homeier, D., Allard, F., & Chabrier, G. 2015, A&A, 577, A42, doi: [10.1051/0004-6361/201425481](https://doi.org/10.1051/0004-6361/201425481)

Billier, B., Lacour, S., Juhász, A., et al. 2012, ApJL, 753, L38, doi: [10.1088/2041-8205/753/2/L38](https://doi.org/10.1088/2041-8205/753/2/L38)

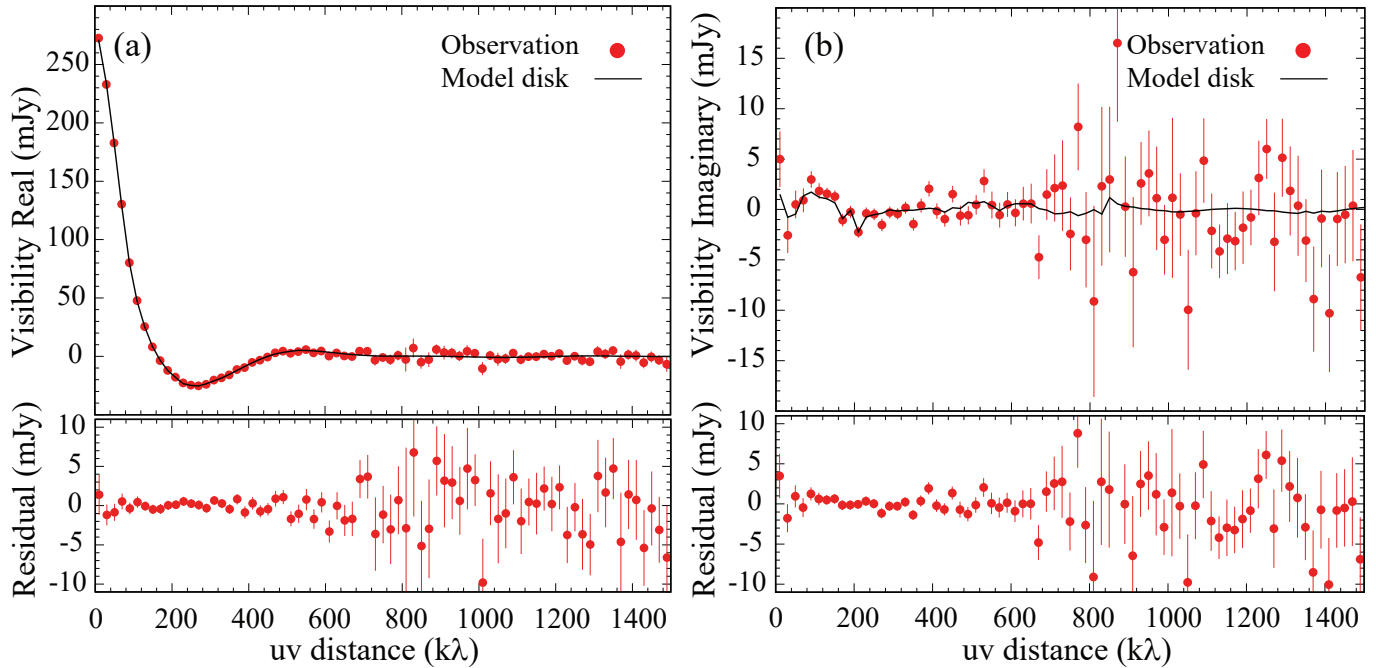


Figure 10. Real (a) and imaginary (b) parts of the visibilities for the observations (red dots) and the best-fit model (black line) in the top panel in visibility analyses in § 4. The bottom panel shows residual visibilities between observations and the best-fit model. The reduced- χ^2 is 1.91.

Calvet, N., Hartmann, L., Kenyon, S. J., & Whitney, B. A. 1994, *ApJ*, 434, 330, doi: [10.1086/174731](https://doi.org/10.1086/174731)

Chang, P., & Oishi, J. S. 2010, *ApJ*, 721, 1593, doi: [10.1088/0004-637X/721/2/1593](https://doi.org/10.1088/0004-637X/721/2/1593)

Cieza, L. A., Casassus, S., Pérez, S., et al. 2017, *ApJL*, 851, L23, doi: [10.3847/2041-8213/aa9b7b](https://doi.org/10.3847/2041-8213/aa9b7b)

Cieza, L. A., González-Ruilova, C., Hales, A. S., et al. 2020, *MNRAS*, doi: [10.1093/mnras/staa3787](https://doi.org/10.1093/mnras/staa3787)

Cutri, R. M., & et al. 2014, *VizieR Online Data Catalog*, II/328

Cutri, R. M., Skrutskie, M. F., van Dyk, S., et al. 2003, *VizieR Online Data Catalog*, II/246

Di Francesco, J., Johnstone, D., Kirk, H., MacKenzie, T., & Ledwosinska, E. 2008, *ApJS*, 175, 277, doi: [10.1086/523645](https://doi.org/10.1086/523645)

Dong, R., Li, S., Chiang, E., & Li, H. 2018a, *ApJ*, 866, 110, doi: [10.3847/1538-4357/aadadd](https://doi.org/10.3847/1538-4357/aadadd)

Dong, R., Rafikov, R., Zhu, Z., et al. 2012, *ApJ*, 750, 161, doi: [10.1088/0004-637X/750/2/161](https://doi.org/10.1088/0004-637X/750/2/161)

Dong, R., Liu, S.-y., Eisner, J., et al. 2018b, *ApJ*, 860, 124, doi: [10.3847/1538-4357/aac6cb](https://doi.org/10.3847/1538-4357/aac6cb)

Dressing, C. D., & Charbonneau, D. 2015, *ApJ*, 807, 45, doi: [10.1088/0004-637X/807/1/45](https://doi.org/10.1088/0004-637X/807/1/45)

Dullemond, C. P., Dominik, C., & Natta, A. 2001, *ApJ*, 560, 957, doi: [10.1086/323057](https://doi.org/10.1086/323057)

Dullemond, C. P., Birnstiel, T., Huang, J., et al. 2018, *ApJL*, 869, L46, doi: [10.3847/2041-8213/aaf742](https://doi.org/10.3847/2041-8213/aaf742)

Durisen, R. H., Boss, A. P., Mayer, L., et al. 2007, in *Protostars and Planets V*, ed. B. Reipurth, D. Jewitt, & K. Keil, 607. <https://arxiv.org/abs/astro-ph/0603179>

Foreman-Mackey, D., Hogg, D. W., Lang, D., & Goodman, J. 2013, *PASP*, 125, 306, doi: [10.1086/670067](https://doi.org/10.1086/670067)

Francis, L., & van der Marel, N. 2020, arXiv e-prints, arXiv:2003.00079. <https://arxiv.org/abs/2003.00079>

Fukagawa, M., Tsukagoshi, T., Momose, M., et al. 2013, *PASJ*, 65, L14, doi: [10.1093/pasj/65.6.L14](https://doi.org/10.1093/pasj/65.6.L14)

Furlan, E., Luhman, K. L., Espaillat, C., et al. 2011, *ApJS*, 195, 3, doi: [10.1088/0067-0049/195/1/3](https://doi.org/10.1088/0067-0049/195/1/3)

Gaia Collaboration, Brown, A. G. A., Vallenari, A., et al. 2020, arXiv e-prints, arXiv:2012.01533. <https://arxiv.org/abs/2012.01533>

Garufi, A., Benisty, M., Pinilla, P., et al. 2018, *A&A*, 620, A94, doi: [10.1051/0004-6361/201833872](https://doi.org/10.1051/0004-6361/201833872)

Gillon, M., Jehin, E., Lederer, S. M., et al. 2016, *Nature*, 533, 221, doi: [10.1038/nature17448](https://doi.org/10.1038/nature17448)

Hashimoto, J., Muto, T., Dong, R., et al. 2021, arXiv e-prints, arXiv:2102.05905. <https://arxiv.org/abs/2102.05905>

Hashimoto, J., Dong, R., Kudo, T., et al. 2012, *ApJL*, 758, L19, doi: [10.1088/2041-8205/758/1/L19](https://doi.org/10.1088/2041-8205/758/1/L19)

Herczeg, G. J., & Hillenbrand, L. A. 2014, *ApJ*, 786, 97, doi: [10.1088/0004-637X/786/2/97](https://doi.org/10.1088/0004-637X/786/2/97)

Johnson, J. A., Aller, K. M., Howard, A. W., & Crepp, J. R. 2010, *PASP*, 122, 905, doi: [10.1086/655775](https://doi.org/10.1086/655775)

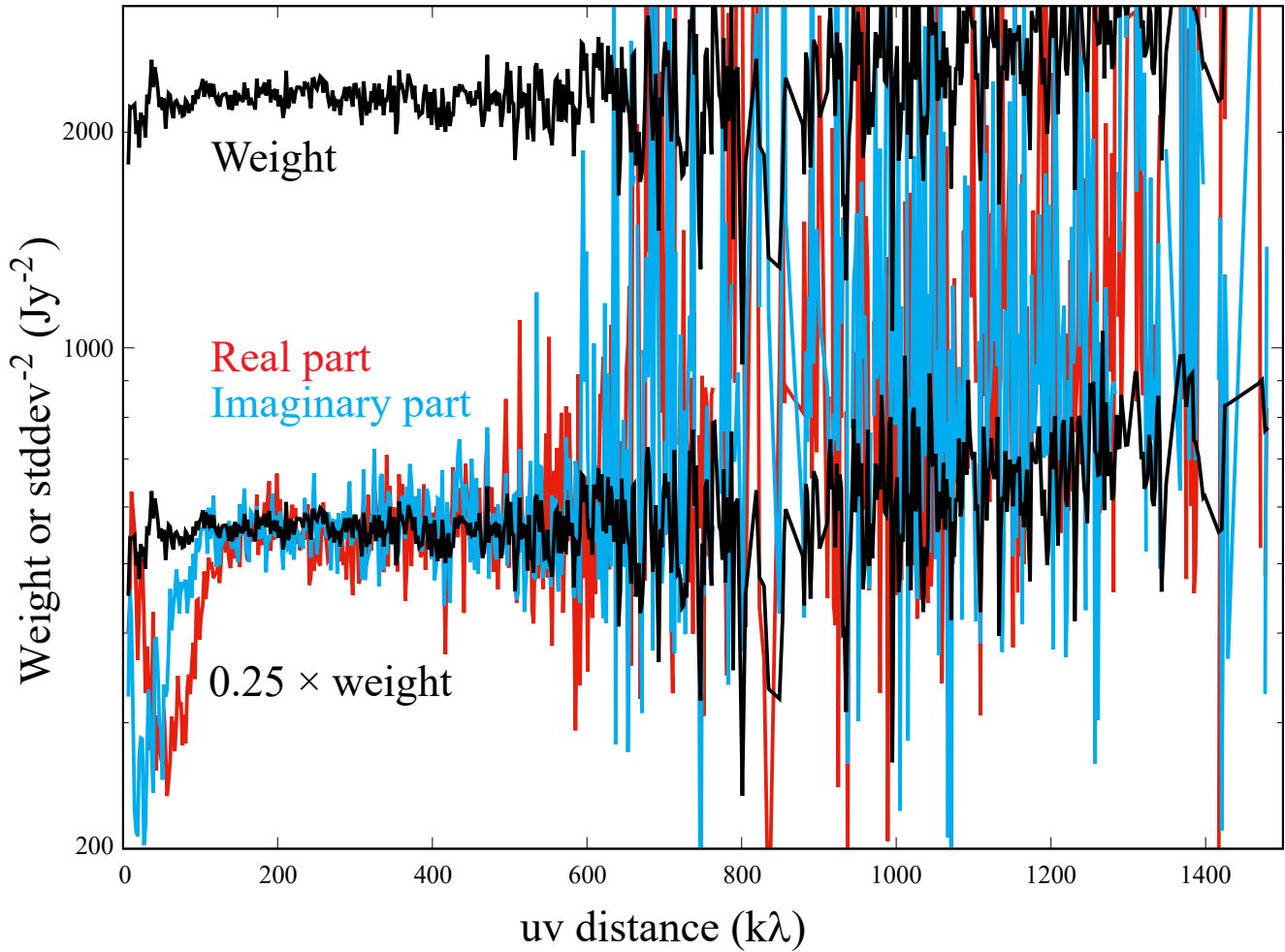


Figure 11. Comparison of weights and standard deviations (stddev) in real and imaginary parts. The weights are typically $4.0\times$ higher than $1/\text{stddev}^2$ of the real and imaginary parts at 100–600 $k\lambda$.

Kanagawa, K. D., Hashimoto, J., Muto, T., et al. 2021, arXiv e-prints, arXiv:2101.10550.

<https://arxiv.org/abs/2101.10550>

Keppler, M., Teague, R., Bae, J., et al. 2019, *A&A*, 625, A118, doi: [10.1051/0004-6361/201935034](https://doi.org/10.1051/0004-6361/201935034)

Kounkel, M., Covey, K., Moe, M., et al. 2019, *AJ*, 157, 196, doi: [10.3847/1538-3881/ab13b1](https://doi.org/10.3847/1538-3881/ab13b1)

Kraus, S., Kreplin, A., Fukugawa, M., et al. 2017, *ApJL*, 848, L11, doi: [10.3847/2041-8213/aa8edc](https://doi.org/10.3847/2041-8213/aa8edc)

Kurtovic, N. T., Pinilla, P., Long, F., et al. 2020, arXiv e-prints, arXiv:2012.02225.

<https://arxiv.org/abs/2012.02225>

Li, Y.-P., Li, H., Li, S., et al. 2020, *ApJL*, 892, L19, doi: [10.3847/2041-8213/ab7fb2](https://doi.org/10.3847/2041-8213/ab7fb2)

Liu, B., Lambrechts, M., Johansen, A., & Liu, F. 2019, *A&A*, 632, A7, doi: [10.1051/0004-6361/201936309](https://doi.org/10.1051/0004-6361/201936309)

Liu, B., Lambrechts, M., Johansen, A., Pascucci, I., & Henning, T. 2020, *A&A*, 638, A88,

doi: [10.1051/0004-6361/202037720](https://doi.org/10.1051/0004-6361/202037720)

Long, F., Pinilla, P., Herczeg, G. J., et al. 2018, *ApJ*, 869, 17, doi: [10.3847/1538-4357/aae8e1](https://doi.org/10.3847/1538-4357/aae8e1)

Loomis, R. A., Öberg, K. I., Andrews, S. M., & MacGregor, M. A. 2017, *ApJ*, 840, 23, doi: [10.3847/1538-4357/aa6c63](https://doi.org/10.3847/1538-4357/aa6c63)

Manara, C. F., Robberto, M., Da Rio, N., et al. 2012, *ApJ*, 755, 154, doi: [10.1088/0004-637X/755/2/154](https://doi.org/10.1088/0004-637X/755/2/154)

Marino, S., Perez, S., & Casassus, S. 2015, *ApJL*, 798, L44, doi: [10.1088/2041-8205/798/2/L44](https://doi.org/10.1088/2041-8205/798/2/L44)

Matsumoto, Y., Gu, P.-G., Kokubo, E., Oshino, S., & Omiya, M. 2020, *A&A*, 642, A23,

doi: [10.1051/0004-6361/202038332](https://doi.org/10.1051/0004-6361/202038332)

Mayama, S., Akiyama, E., Panić, O., et al. 2018, *ApJL*, 868, L3, doi: [10.3847/2041-8213/aae88b](https://doi.org/10.3847/2041-8213/aae88b)

- McMullin, J. P., Waters, B., Schiebel, D., Young, W., & Golap, K. 2007, in *Astronomical Society of the Pacific Conference Series*, Vol. 376, *Astronomical Data Analysis Software and Systems XVI*, ed. R. A. Shaw, F. Hill, & D. J. Bell, 127
- Miguel, Y., Cridland, A., Ormel, C. W., Fortney, J. J., & Ida, S. 2020, *MNRAS*, 491, 1998, doi: [10.1093/mnras/stz3007](https://doi.org/10.1093/mnras/stz3007)
- Monet, D. G., Levine, S. E., Canzian, B., et al. 2003, *AJ*, 125, 984, doi: [10.1086/345888](https://doi.org/10.1086/345888)
- Morales, J. C., Mustill, A. J., Ribas, I., et al. 2019, *Science*, 365, 1441, doi: [10.1126/science.aax3198](https://doi.org/10.1126/science.aax3198)
- Ormel, C. 2017, in *10th RESCEU/Planet2 Symposium Planet Formation around Snowline*, E5
- Ormel, C. W., & Liu, B. 2018, *A&A*, 615, A178, doi: [10.1051/0004-6361/201732562](https://doi.org/10.1051/0004-6361/201732562)
- Papaloizou, J. C. B., Nelson, R. P., Kley, W., Masset, F. S., & Artymowicz, P. 2007, in *Protostars and Planets V*, ed. B. Reipurth, D. Jewitt, & K. Keil, 655. <https://arxiv.org/abs/astro-ph/0603196>
- Pérez, L. M., Benisty, M., Andrews, S. M., et al. 2018, *ApJL*, 869, L50, doi: [10.3847/2041-8213/aaf745](https://doi.org/10.3847/2041-8213/aaf745)
- Pugh, E. M., & Winslow, G. H. 1966, *The analysis of physical measurements* (Reading, MA: Addison-Wesley)
- Raettig, N., Klahr, H., & Lyra, W. 2015, *ApJ*, 804, 35, doi: [10.1088/0004-637X/804/1/35](https://doi.org/10.1088/0004-637X/804/1/35)
- Ragusa, E., Dipierro, G., Lodato, G., Laibe, G., & Price, D. J. 2017, *MNRAS*, 464, 1449, doi: [10.1093/mnras/stw2456](https://doi.org/10.1093/mnras/stw2456)
- Ribas, Á., Espaillat, C. C., Macías, E., et al. 2017, *ApJ*, 849, 63, doi: [10.3847/1538-4357/aa8e99](https://doi.org/10.3847/1538-4357/aa8e99)
- Rosenfeld, K. A., Chiang, E., & Andrews, S. M. 2014, *ApJ*, 782, 62, doi: [10.1088/0004-637X/782/2/62](https://doi.org/10.1088/0004-637X/782/2/62)
- Testi, L., Birnstiel, T., Ricci, L., et al. 2014, in *Protostars and Planets VI*, ed. H. Beuther, R. S. Klessen, C. P. Dullemond, & T. Henning, 339, doi: [10.2458/azu_uapress_9780816531240-ch015](https://doi.org/10.2458/azu_uapress_9780816531240-ch015)
- Toomre, A. 1964, *ApJ*, 139, 1217, doi: [10.1086/147861](https://doi.org/10.1086/147861)
- Tsukagoshi, T., Muto, T., Nomura, H., et al. 2019, *ApJL*, 878, L8, doi: [10.3847/2041-8213/ab224c](https://doi.org/10.3847/2041-8213/ab224c)
- van der Marel, N., Cazzoletti, P., Pinilla, P., & Garufi, A. 2016, *ApJ*, 832, 178, doi: [10.3847/0004-637X/832/2/178](https://doi.org/10.3847/0004-637X/832/2/178)
- van der Marel, N., Birnstiel, T., Garufi, A., et al. 2020, *arXiv e-prints*, arXiv:2010.10568. <https://arxiv.org/abs/2010.10568>
- van der Plas, G., Wright, C. M., Ménard, F., et al. 2017, *A&A*, 597, A32, doi: [10.1051/0004-6361/201629523](https://doi.org/10.1051/0004-6361/201629523)
- White, R. J., & Hillenbrand, L. A. 2004, *ApJ*, 616, 998, doi: [10.1086/425115](https://doi.org/10.1086/425115)
- Whitney, B. A., & Hartmann, L. 1993, *ApJ*, 402, 605, doi: [10.1086/172163](https://doi.org/10.1086/172163)
- Whitney, B. A., Robitaille, T. P., Bjorkman, J. E., et al. 2013, *ApJS*, 207, 30, doi: [10.1088/0067-0049/207/2/30](https://doi.org/10.1088/0067-0049/207/2/30)
- Zhang, K., Bergin, E. A., Blake, G. A., et al. 2016, *ApJL*, 818, L16, doi: [10.3847/2041-8205/818/1/L16](https://doi.org/10.3847/2041-8205/818/1/L16)
- Zhu, Z. 2019, *MNRAS*, 483, 4221, doi: [10.1093/mnras/sty3358](https://doi.org/10.1093/mnras/sty3358)